AIP Review of Scientific Instruments

Novel high-temperature and pressure-compatible ultrasonic levitator apparatus coupled to Raman and Fourier transform infrared spectrometers

Stephen J. Brotton and Ralf I. Kaiser

Citation: Rev. Sci. Instrum. **84**, 055114 (2013); doi: 10.1063/1.4804647
View online: http://dx.doi.org/10.1063/1.4804647
View Table of Contents: http://rsi.aip.org/resource/1/RSINAK/v84/i5
Published by the AIP Publishing LLC.

Additional information on Rev. Sci. Instrum.

Journal Homepage: http://rsi.aip.org
Journal Information: http://rsi.aip.org/about/about_the_journal
Top downloads: http://rsi.aip.org/features/most_downloaded
Information for Authors: http://rsi.aip.org/authors

ADVERTISEMENT

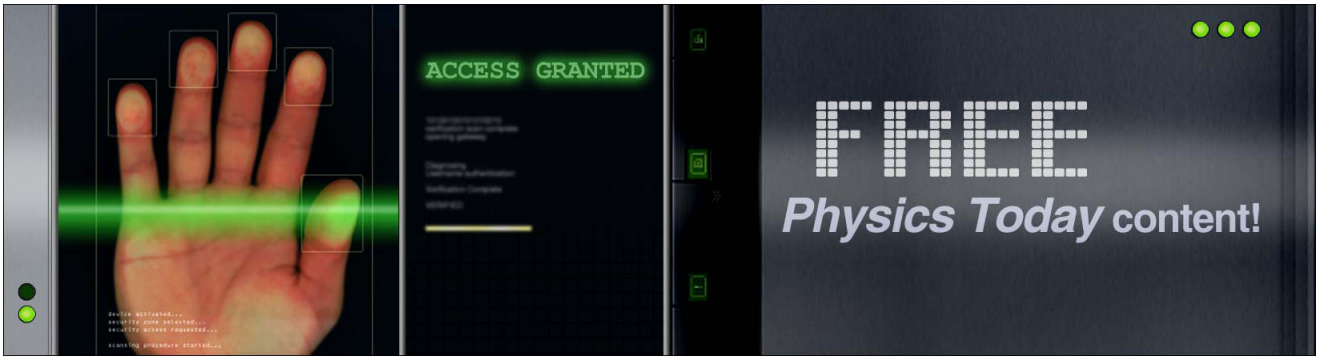

Downloaded 13 Jun 2013 to 128.171.57.189. This article is copyrighted as indicated in the abstract. Reuse of AIP content is subject to the terms at: http://rsi.aip.org/about/rights_and_permissions

Novel high-temperature and pressure-compatible ultrasonic levitator apparatus coupled to Raman and Fourier transform infrared spectrometers

Stephen J. Brotton[1,2] and Ralf I. Kaiser[1,2]
[1]*Department of Chemistry, University of Hawaii at Manoa, Honolulu, Hawaii 96822, USA*
[2]*NASA Astrobiology Institute, University of Hawaii at Manoa, Honolulu, Hawaii 96822, USA*

(Received 18 February 2013; accepted 29 April 2013; published online 29 May 2013)

We describe an original apparatus comprising of an acoustic levitator enclosed within a pressure-compatible process chamber. To characterize any chemical and physical modifications of the levitated particle, the chamber is interfaced to complimentary, high-sensitivity Raman (4390–170 cm^{-1}), and Fourier transform infrared (FTIR) (10 000–500 cm^{-1}) spectroscopic probes. The temperature of the levitated particle can be accurately controlled by heating using a carbon dioxide laser emitting at 10.6 μm. The advantages of levitating a small particle combined with the two spectroscopic probes, process chamber, and infrared laser heating makes novel experiments possible relevant to the fields of, for example, planetary science, astrobiology, and combustion chemistry. We demonstrate that this apparatus is well suited to study the dehydration of a variety of particles including minerals and biological samples; and offers the possibility of investigating combustion processes involving micrometer-sized particles such as graphite. Furthermore, we show that the FTIR spectrometer enables the study of chemical reactions on the surfaces of porous samples and scientifically and technologically relevant, micrometer-thick levitated sheets. The FTIR spectrometer can also be used to investigate non-resonant and resonant scattering from small, irregularly-shaped particles across the mid-infrared range from 2.5 μm to 25 μm, which is relevant to scattering from interplanetary dust and biological, micrometer-sized samples but cannot be accurately modelled using Mie theory.
© *2013 AIP Publishing LLC*. [http://dx.doi.org/10.1063/1.4804647]

I. INTRODUCTION

During the past few decades, acoustic levitation[1] has been exploited in a diverse range of applications including analytical chemistry, astrochemistry, material science, and medicinal chemistry.[2,3] In acoustic levitation, intense sound waves, which are produced by an ultrasonic-piezoelectric radiator, reflect from a planar or concave-shaped solid plate to generate a standing wave. The sound waves produce acoustic radiation pressure on the particle, and the resultant acoustic force counteracts the gravitational force.[4] Particles are therefore levitated slightly below the pressure nodes of the ultrasonic standing wave. Levitation has the advantage of avoiding the complicating effects of a contacting surface, and so permits the so-called *container-less processing* of a single, levitated particle. The absence of walls also increases the sensitivity of the spectroscopic detection techniques such as Raman spectroscopy, Fourier transform infrared (FTIR) spectroscopy, and X-ray diffraction utilized to study the chemical and physical modifications of the levitated particle. Furthermore, a levitator can be used to probe the differences between the physical and chemical processes on the bulk samples typically used in surface science and the surfaces of micrometer-sized levitated particles.[5,6] Finally, owing to their small total heat capacity, the levitated particle can be heated to a high temperature (see Sec. II C) over very short time scales and be cooled more rapidly (see Subsection 3 of the Appendix) thus allowing precise control of the sample temperature.

Alternative experimental techniques have been developed to trap and study micrometer- or even nanometer-sized particles. These include Paul-type ion traps,[7] optical trapping utilizing lasers,[8] aerodynamic levitation,[9] diamagnetic levitation,[10] and electrostatic levitation.[11] Electric and laser traps are sensitive to the physical properties of the samples, however, such as the electric charge (Paul trap, electrostatic levitation) and refractive index (laser trap). In contrast, acoustic radiation pressure is *independent* of the refractive index and charge and so can be used as a versatile trap to levitate most liquid and solid substances.

Here, we report on the development of a new apparatus combining an acoustic levitator with a pressure-compatible process chamber, heating by a carbon dioxide laser, and characterization of the chemical and physical modifications of the levitated particles simultaneously via FTIR (10 000–500 cm^{-1}) and Raman spectroscopy (4390–170 cm^{-1}). Acoustic levitation has previously been combined separately with Raman spectroscopy,[12–14] a FTIR spectrometer,[15] and a carbon dioxide laser;[16,17] but, to our knowledge, all three techniques have not been combined simultaneously into a single, pressure-compatible apparatus. Raman scattering and infrared absorption spectroscopy provide complimentary information on the rovibrational modes of molecules. In FTIR absorption spectroscopy, the electric dipole transitions cause a change of parity of the atom or molecule and the selection rule is $\Delta J = 0, \pm 1$, where J is total angular momentum. Conversely, Raman scattering does not change the parity and the selection rules are given by $\Delta J = 0, \pm 2$. A Raman transition consequently does not require a permanent electric dipole moment, and so Raman lines are observed for symmetric molecules. In contrast to FTIR spectroscopy, Raman spectroscopy therefore has the advantage of detecting homonuclear diatomic species such as the

 © 2013 AIP Publishing LLC

Downloaded 13 Jun 2013 to 128.171.57.189. This article is copyrighted as indicated in the abstract. Reuse of AIP content is subject to the terms at: http://rsi.aip.org/about/rights_and_permissions

important interstellar molecules H_2, O_2, N_2, and C_2. The sharpness and intensity of the Raman spectral features for minerals and organic molecules and additionally the ability to observe the Raman-active symmetric stretching modes of aromatic rings are further complementary aspects to infrared absorption spectroscopy.

The combination of the complimentary Raman and FTIR spectroscopic probes, the pressure-compatible process chamber, heating by a carbon dioxide laser, and the advantages of levitating very small particles makes novel experiments possible, which could not have been conducted previously relevant to the fields of, for instance, planetary science, astrobiology, and combustion chemistry. To demonstrate the performance of the experimental apparatus, test cases of four new research directions are described in this paper. First, of importance to the planetary sciences,[18–21] we study the stepwise dehydration of levitated epsomite ($MgSO_4 \cdot 7H_2O$) and gypsum ($CaSO_4 \cdot 2H_2O$) crystals induced by heating from the carbon dioxide laser and identify *in situ* the distinct hydration states, namely, magnesium sulfate ($MgSO_4 \cdot nH_2O$; n = 7, 6, …, 0), bassanite ($CaSO_4 \cdot 0.5H_2O$), and anhydrite ($CaSO_4$). Second, considering astrobiology, we investigate the reaction pathways induced by heating levitated samples of biological relevance such as the amino acid cysteine ($HSCH_2CH_2CNH_2COOH$). Third, in view of our goal to study combustion processes[22–24] and the growth of organics on carbonaceous particles, a graphite grain can be heated by a carbon dioxide laser to elevated temperatures,[16,17] thereby enabling the heated particle to react with the process gases such as oxygen, nitrogen, or hydrocarbon gas. Fourth, the introduction of the FTIR spectrometer enables the study of the scattering of light by small, irregularly shaped particles, such as the organic polymers considered here, where Mie theory does not accurately predict the scattering functions.[25] Although a dominant scattering background and distortion of the absorption lines is expected in the FTIR spectra of acoustically levitated particles, both spherical and irregular, we have found microgram samples that produce relatively undistorted spectra such as tens of micrometer thick sheets. Thus, the FTIR spectrometer can be applied to determine the molecular composition of such samples and, hence, study reactions on their surfaces. There are many potential applications, both scientific and technological, for determining the chemical modifications on the surfaces of thin, levitated sheets. For example, in recent years there has been considerable interest in graphene sheets, and a hindrance to graphene chemistry research has been a lack of samples suitable for study.[26]

II. EXPERIMENTAL APPARATUS

A. Ultrasonic levitator

The levitator device was adapted from a Tec5 AG-type acoustic levitator and is depicted in Figs. 1 and 2. Ultrasonic sound waves are generated by a piezoelectric transducer, which oscillates at 58 kHz producing a wavelength, λ, of about 5.9 mm in air at standard temperature (20 °C) and pressure (1 atm). The amplitude of the transducer's oscillations can be varied using a potentiometer, which enables the radio frequency (RF) power input to be adjusted between 0.7 and 5.0 W. The multiple reflections of the sound waves between the transducer and the concave-shaped reflector generate a standing wave. The pressure amplitude of the standing wave was monitored by connecting the output of a piezoelectric sensor to an oscilloscope. In accordance with Bernoulli's theorem, the maxima in the (time-averaged) kinetic energy density of the standing wave, $\rho\langle v^2\rangle/2$, correspond to minima in the pressure.[27] Owing to the resulting acoustic radiation pressure and the counteracting gravitational force, solid or liquid samples are levitated slightly below the pressure minima of the ultrasonic standing wave. The acoustic radiation pressure is much larger for the present standing wave produced within a resonant cavity than for a traveling wave. The largest diameter of particles that can be levitated in the present levitator is approximately 2.5 mm, whereas the smallest is around 15 μm. A micrometer manipulator allows the distance between the transducer plate and the reflector to be adjusted to an integral number of half wavelengths, so that the resonance conditions can be maintained following any changes in the gas composition, temperature, or pressure. The distance between the front plate of the transducer and the reflector is usually set to 2.5λ giving 5 pressure minima. The plate separation can be optimized from outside of the process chamber using an external rotary manipulator attached to the top flange; the rotary manipulator connects to the micrometer on the levitator via a separable coupling device inside of the process chamber. Owing to the curved reflector, the ultrasonic waves are not planar but slightly concave. The resulting horizontal (or transverse) component of the sound velocity produces a horizontal, radial restoring force, which centers the particle on the levitator's axis.[4] For stability considerations, for the present single-axis levitator, we note that the horizontal force is approximately one order of magnitude smaller than the vertical, axial force.

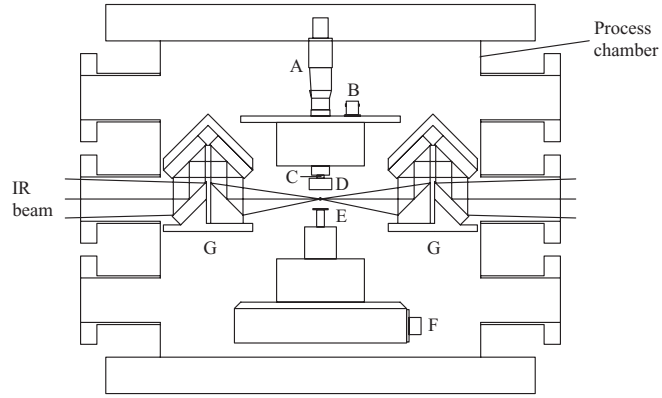

FIG. 1. Schematic diagram of the levitator (A–F), second stage optics (G), and process chamber. Ultrasonic sound waves are generated by the piezoelectric transducer (E). Owing to multiple reflections between the transducer and the concave reflector (D), a standing wave is generated. A micrometer (A) allows the distance between the front plate of the transducer and the reflector to be adjusted to an integral number of half wavelengths. The pressure amplitude of the standing wave is monitored by connecting the output of the piezoelectric sensor (C) via connector (B) to an oscilloscope. The RF power to the transducer is input via connector F. For clarity, the supports for the levitator and second stage optics are not shown.

Downloaded 13 Jun 2013 to 128.171.57.189. This article is copyrighted as indicated in the abstract. Reuse of AIP content is subject to the terms at: http://rsi.aip.org/about/rights_and_permissions

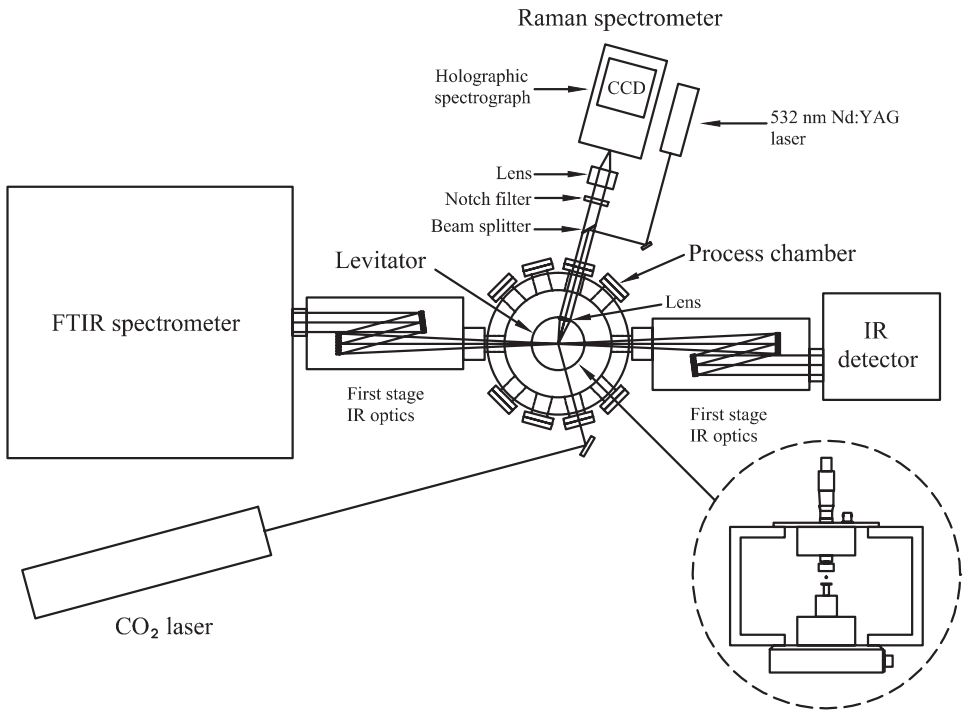

FIG. 2. Top view of the levitator apparatus displaying the ultrasonic levitator, process chamber, carbon dioxide laser, Raman spectrometer, FTIR spectrometer, IR detector, and the first stage optics. The inset shows the levitator including the supports in more detail.

The particles are placed in the central pressure node by using a magnetically-coupled wobble stick, which is fixed to a side port of the process chamber. A section of high-transparency (88% open) stainless-steel wire mesh with dimensions of 16 mm × 24 mm is attached to the end of the wobble stick by a thin wire frame to form a highly moveable, acoustically transparent spatula inside of the process chamber. The particles to be levitated are placed on the wire mesh. The chamber is then evacuated (using an oil-free turbo molecular pump backed by a hydrocarbon-free diaphragm pump) and subsequently filled with the required process or inert gas. The wobble stick is moved inwards to place the particle in the central pressure node, after which the wire mesh is lowered and finally retracted to leave a levitated particle.

B. Process chamber

The levitator device is enclosed within a pressure-compatible process chamber, which allows control of the gas temperature, pressure, and chemical composition to permit experiments related to planetary chemistry, biochemistry, material science, atmospheric chemistry, and combustion processes. The pressure as measured by a MKS 626B series capacitance manometer can be varied over the full range of operation of the levitator from a few hundred to a few thousand Torr; the experiments described in the present paper were performed at 1 atm pressure (760 Torr). The chamber allows levitation in an inert or anhydrous gas. Alternatively, we can introduce highly reactive gases to study reactions between the gas and the levitated particle, possibly enhanced by heating from the carbon dioxide laser. The chamber is UHV compatible and so can safely contain any toxic gases. The gas temperature in the locality of the levitated particle was measured using a silicon-diode temperature sensor, which covers the range from 1.4 to 500 K, and a Lake Shore model 333 temperature controller. The sensor is attached to the end of a UHV linear positioner, so that it can be withdrawn from the trap center before levitating a particle.

C. Heating the levitated particles

To heat the levitated particle, we used a 40 W carbon dioxide laser emitting at 10.6 μm purchased from Synrad, Inc. The output power of the laser can be adjusted between 1 W and 40 W by varying the duty cycle of the discharge. The pulse width modulation (PWM) frequency can be set to 5, 10, or 20 kHz. At the 20 kHz used here, the output power is essentially continuous with only a small ripple present. A planar copper mirror and zinc selenide (ZnSe) windows on the chamber are used to transport the infrared beam to the levitated particle, which is located 104 cm from the exit of the laser as measured along the path of the beam. The diameter of the beam exiting the laser is 2.5 ± 0.5 mm ($1/e^2$) and the beam divergence (full angle) less than 7.0 mR. Consequently, the diameter of the laser beam at the trap center is approximately 10 mm, which facilitates aligning the beam on the particle. The arrangement of the infrared optics for the carbon dioxide laser beam is shown in Fig. 2. When heated by the carbon dioxide laser, the particle usually spins rapidly around the central, vertical axis of the levitator. Therefore, although the irradiation is from one side of the chamber only, all surfaces of the particle are heated resulting in a homogeneous sample temperature. The temperature of the levitated particles can be calculated using the requirement that, in thermal equilibrium, the radiation power absorbed from the carbon dioxide laser and surroundings equals the power radiated by the particle

Downloaded 13 Jun 2013 to 128.171.57.189. This article is copyrighted as indicated in the abstract. Reuse of AIP content is subject to the terms at: http://rsi.aip.org/about/rights_and_permissions

plus the heat loss by conduction (see the Appendix). A spectrometer will be incorporated to determine the temperature of the particle via its black-body spectrum. The heating of the air around the particle places an upper limit on the maximum temperature achievable for acoustically levitated particles.[28] Experiments have, nevertheless, been conducted at temperatures up to 2700 K using an aero-acoustic levitator with ultrasonic transducers on three orthogonal axes.[17]

D. Raman spectrometer

A schematic diagram of the Raman spectrometer is included in Fig. 2. The Raman transitions are excited by the 532 nm line of a diode-pumped, Q-switched Nd:YAG laser. The laser beam has a diameter of 0.35 mm ($1/e^2$) and a divergence of 3.8 mrad (full angle). The average power output of the laser can be varied by changing the pulse repetition rate between a few Hz and 200 kHz using an external pulse generator. At a typical frequency of 1 kHz, the average power output is 200 mW and the pulse width 13.5 ns. To avoid heating by the Raman laser, for some samples the frequency was reduced to 100 Hz. As Fig. 2 shows, a dichroic beam splitter reflects the laser beam, which is incident at 45° relative to the surface normal, towards the sample but transmits the longer Raman shifted wavelengths of the backscattered photons. A lens with a focal length of 60 mm focuses the laser beam onto the sample and, by increasing the collection solid angle of the backscattered photons, significantly improves the count rate. In addition to the beam splitter, a 532 nm notch holographic filter prevents the intense 532 nm Rayleigh scattered beam from reaching and damaging the charge-coupled device (CCD) camera. The backscattering geometry serves to maximize the Raman signal obtained from the levitated particle. The Raman shifted, backscattered photons are focused by a 50 mm *f*/1.8 D camera lens through a slit into a HoloSpec $f/1.8$ holographic imaging spectrograph. The slit has a width of 100 μm which gives a resolution of 9 cm^{-1}. To maximize the transmission of the beam through the slit, the position of the camera lens was optimized using an x, y, z manipulator. After passing through the slit, the diverging beam is collimated by a lens towards two overlaid holographic transmission gratings. One grating disperses the low Raman shift wavenumbers from 2388 to 168 cm^{-1}, whereas the other separates the higher Raman shifts in the 4387–2265 cm^{-1} range. The light from the two Raman shift ranges is focused onto spatially distinct halves of a PI-Max 2 ICCD (intensified charge-coupled device) camera from Princeton Instruments. The CCD camera is thermoelectrically cooled, gated (see below), and composed of 1024 × 256 pixels. The final spectra for each spectral range are obtained by summing the total counts recorded in each pixel perpendicular to the dispersion axis. The spectrometer thus simultaneously covers the spectral range from 4387 to 168 cm^{-1}. The Raman shift scale was calibrated using cyclohexane and is estimated to be accurate to within 1 cm^{-1}.

When irradiated by a laser, some samples, especially those containing organics, produce significant fluorescence which can dominate over the Raman signal. The fluorescence is particularly large for excitation by a 532 nm laser. The fluorescent background can be reduced using the pulsed laser and gated detector described above. By varying, first, the time delay between the laser pulse and opening the gate to collect the CCD signal (gate delay) and, second, the period for which the gate is open (period), it is possible to detect the faster Raman signal whilst rejecting most of the longer-lived fluorescence. For the present experimental arrangement, typical values for the gate delay and period are 500 ns and 50 ns, respectively, as measured relative to the triggering pulse sent simultaneously to the laser and CCD gate. The timing sequence also enables spectra to be collected in bright light conditions. Additional details of the Raman spectrometer are given in Ref. 29.

E. FTIR spectrometer

1. Theoretical background

The interaction between electromagnetic radiation and a dielectric sphere with a radius r comparable to the wavelength λ causes strong scattering, which can be modeled using Mie scattering theory.[25] In FTIR spectroscopy, Mie scattering produces broad sinusoidal-like oscillations in the baseline of the spectra, which can cause inaccuracies when measuring the position and intensity of absorption lines. Mie scattering can be approximated by the equation

$$Q = 2 - \frac{4}{p}\sin p + \frac{4}{p^2}(1 - \cos p), \tag{1}$$

where Q is the cross section per unit area (area $= 4\pi r^2$), $p = 4\pi r\ (n - 1)/\lambda$ is the phase difference between a ray that passes through the center of the sphere and one following the same path without the sphere present, and n is the ratio of the refractive indices inside the sphere and the surrounding medium. Resonant Mie scattering occurs when the wavelength passes through an absorption band. Consequently, absorption lines have an asymmetric shape, and a sharp decrease is observed on the high wavenumber side of the band. Resonant Mie scattering can significantly affect the position, shape, and intensity of an absorption band, which makes it difficult to recover the undistorted absorption spectrum and, hence, identify the chemical species producing the FTIR spectrum.

The absorption Q_{abs} and scattering Q_{sca} efficiencies for a small sphere vary as[25]

$$Q_{abs} \propto r/\lambda, \quad Q_{sca} \propto (r/\lambda)^4. \tag{2}$$

Therefore, scattering dominates over absorption unless the particle is small compared to the wavelength, that is, $r \ll \lambda$, which corresponds to the Rayleigh scattering limit. The shortest wavelength observable with the present FTIR spectrometer is 2.5 μm, and so the particle diameter, d, would need to be significantly smaller than 2.5 μm for absorption to dominate across the full observable spectral range (2.5 μm $< \lambda <$ 25 μm). For particles with diameters that can be levitated in the present apparatus (15 μm $< d <$ 2.5 mm), scattering consequently dominates over absorption. Thus, for a spherical particle, one does not observe undistorted absorption lines, but asymmetric bands superimposed upon a large Mie scattering background.

Downloaded 13 Jun 2013 to 128.171.57.189. This article is copyrighted as indicated in the abstract. Reuse of AIP content is subject to the terms at: http://rsi.aip.org/about/rights_and_permissions

Mie calculations accurately predict the non-resonant scattering produced by a sphere. However, Mie theory does not accurately represent the scattering functions of highly irregularly shaped particles or the Mie resonances produced by absorption lines. Laboratory experiments are therefore needed to obtain the scattering functions of non-spherical particles. Such measurements are relevant to scattering from, for example, interplanetary dust including meteorite fragments, Brownlee particles, and comet dust tails.[30] There is also considerable interest in removing the effects of Mie scattering to obtain undistorted spectra of biological, micrometer-sized samples.[31] Weiss-Wrana[30] used an electrostatic levitator and a He–Ne laser emitting at the fixed wavelength of 633 nm to measure the cross sections of irregularly shaped particles as a function of the scattering angle. In contrast, as discussed below, we scan across the mid-infrared range from 2.5 μm to 25 μm and so observe the variation in the cross section with wavelength including the Mie resonances.

2. FTIR experimental apparatus

We use a Thermo Scientific Nicolet 6700 FTIR spectrometer. The infrared (IR) beam emerging from the FTIR spectrometer has a diameter of approximately 50 mm. To increase the detection efficiency, it is clearly necessary to reduce the diameter of the IR beam in the region of the levitated particle. The two standard approaches of beam diameter reduction using a Keplerian or Galilean telescope are unsuccessful for the FTIR beam. To understand the reason for this consider, first, that the IR beam diverges widely and is poorly collimated because, rather than the ideal of a point source, the EverGlo IR source within the FTIR spectrometer has a diameter of about 10 mm. Second, note that the output beam divergence θ_o of a beam reducing telescope is given by Eq. (3), where θ_i denotes the input beam divergence and here the magnification, $M, \ll 1$

$$\theta_o = \frac{\theta_i}{M}. \tag{3}$$

Consequently, the beam reducing telescope increases the divergence of an already widely diverging beam and, hence, actually has the effect of enlarging the beam diameter in the trap center. We therefore use an alternative approach involving two stages of beam reduction. The main purpose of the first stage optics, as shown in Fig. 2, is to focus the IR beam through the 33 mm clear-view diameter KBr window towards the levitated particle. In the first stage optics, the beam reflects from a 50.8 mm diameter planar mirror and is then focussed by a 15° off-axis parabolic mirror with a focal length of 517 mm. A 15° mirror was chosen rather than, for example, a 90° off-axis parabolic mirror to avoid obscuring the other ports on the chamber. Gold-coated aluminium mirrors are used for all the IR optics, since the reflectance of 0.98 at the relevant wavelengths is high. To greatly reduce unwanted water and carbon dioxide lines in the FTIR spectra, the first stage optics are enclosed within plexiglass boxes which are purged with CO_2- and H_2O-free air (so-called "dry air"). Owing to the large divergence of the IR beam entering the first stage optics, a small focussed spot was not produced at the trap center but a rectangular image with dimensions of approximately 22 mm × 17 mm. To further reduce the spot size, we used the well-known optical relation

$$\text{spot size} \propto \text{focal length} \times \text{divergence} \tag{4}$$

to deduce that a second focussing mirror should be placed as close as practicable to the trap center, and therefore introduced the second stage of IR optics shown in Fig. 1. In the second stage optics, the beam reflects from three 50.8 mm diameter planar mirrors and is then focussed by a 90° off-axis, 25.4 mm diameter parabolic mirror with a focal length of 76.2 mm to form a spot of 4 mm in diameter. The transmitted radiation subsequently enters an identical optical system in the reverse order (see Figs. 1 and 2), so that the original 50 mm diameter, unfocussed IR beam is recovered before finally entering the IR detector box. The expected transmission following reflection from the 12 gold mirrors composing both optical stages is $0.98^{12} = 0.78$, and therefore the measured value of 0.86 is better than expected. Thus, by two stages of focussing, the detection efficiency has been increased by a factor of approximately 130.

F. Advantages of the experimental apparatus

In this section, we will summarise the advantages of levitating particles in the present experimental apparatus. First, since the levitator is enclosed within a process chamber, the environmental conditions such as the gas pressure and composition can be controlled. Second, the absence of contact between the levitated particle and any external object means that (i) only the required substances affect the chemical reactions, (ii) there are no temperature changes or delays caused by a supporting structure, and (iii) the spectroscopic probes observe the molecules of interest only and, hence, the detection sensitivity is increased. Third, for the present experimental layout with the particle levitated in the center of a process chamber equipped with several side viewports (see Fig. 2), a number of complimentary, high-sensitivity spectroscopic techniques can simultaneously probe for any chemical or physical modifications. Fourth, owing to the small heat capacity, the levitated particles can be heated to high temperatures over very short time scales and be cooled rapidly (see Subsection 3 of the Appendix) thus enabling the accurate temporal control of the sample temperature. Fifth, fine adjustments of the CO_2 laser power permits accurate control of the particle temperature, and the addition of the black-body spectrometer will allow even more precise measurement of the particle temperature. Finally, levitation and the two-stage FTIR optical system are well suited to studying the scattering of electromagnetic radiation from small particles. In addition to these general advantages, the benefits of the present apparatus that apply more specifically to the individual test case experiments are discussed in Sec. III.

III. PERFORMANCE STUDIES AND DISCUSSION

A. Dehydration studies

In addition to the general advantages discussed in Sec. II F, for dehydration studies there are further more

Downloaded 13 Jun 2013 to 128.171.57.189. This article is copyrighted as indicated in the abstract. Reuse of AIP content is subject to the terms at: http://rsi.aip.org/about/rights_and_permissions

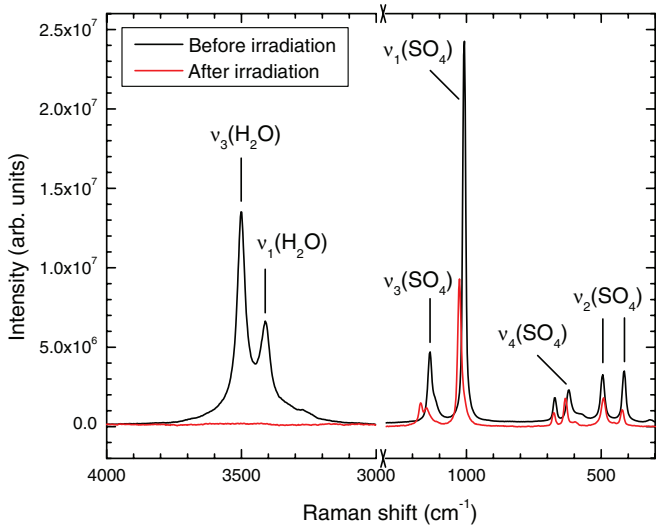

FIG. 3. Alteration in the Raman spectrum when a grain of gypsum ($CaSO_4 \cdot 2H_2O$) levitated in anhydrous nitrogen is dehydrated to anhydrite ($CaSO_4$) by irradiation from a CO_2 laser. The assignments of the $\nu(SO_4)$ and $\nu(H_2O)$ vibrational modes for the gypsum peaks are shown. The corresponding $\nu_1(SO_4)$ and $\nu_3(SO_4)$ vibrational modes in anhydrite are observed at slightly higher Raman shifts (see text for details).

specific benefits of the present apparatus. First, the small particle volume means that dehydration or rehydration processes occur more rapidly than for bulk samples. Second, since the levitator is enclosed within a process chamber, the relative humidity of the gas introduced into the process chamber could be varied using a humidity controller or by mixing anhydrous and water-saturated gas in different combinations.[32]

1. Sulfates

We used the CO_2 laser to heat a gypsum crystal ($CaSO_4 \cdot 2H_2O$) levitated in anhydrous nitrogen gas at atmospheric pressure. Figure 3 shows the change in the Raman spectrum of gypsum following irradiation for several hours at a laser power of 2.0 W, which corresponds to a temperature of around 400 K (see the Appendix). The disappearance of the ν_1 symmetric stretch and ν_3 asymmetric stretch modes of water at 3412 cm^{-1} and 3501 cm^{-1}, respectively, demonstrates that the transition to anhydrite ($CaSO_4$) is complete. The peaks at 1008 cm^{-1} and 1136 cm^{-1} in the unirradiated spectrum are produced by the ν_1 symmetric stretch and ν_3 asymmetric stretch modes of the sulfate anion (SO_4^{2-}), respectively. As a consequence of removing the water molecules, the $\nu_1(SO_4^{2-})$ and $\nu_3(SO_4^{2-})$ peaks reduce in amplitude and shift, respectively, to the higher wavenumbers of 1026 cm^{-1} and 1147 cm^{-1}. Further details of our Raman spectroscopic study of gypsum and epsomite dehydration using an ultrasonic levitator are given in Ref. 6.

2. Cysteine

The levitator apparatus can be used to study the dehydration of the amino acids. For example, when heated two cysteine molecules could link by an oxidation process where two hydrogen atoms are removed and cystine is produced, as illustrated by process (1) in Fig. 4. Alternatively, L-cysteine could dehydrate by process (2) shown in Fig. 4 resulting in the formation of a peptide bond. To determine which of the possibilities (1) or (2) dominates, we used the CO_2 laser to heat a 1 mm diameter L-cysteine crystal levitated in anhydrous nitrogen gas at atmospheric pressure. The changes to the Raman spectrum began to occur more rapidly when the laser power was increased to 4.0 W, which corresponds to a temperature of approximately 490 K. In Fig. 5 (top), the L-cysteine spectrum following irradiation at 3.8 W or approximately 480 K for 52 min and 490 K for 3 h 27 min is compared with the L-cysteine spectrum before irradiation. The L-cysteine Raman bands have been assigned spectroscopically by Pawlukojc *et al.*[33] For reference, a D-cystine spectrum is shown in Fig. 5 (bottom). The vibrational assignments of the Raman bands in cystine are given in Ref. 34. The new peak at 515 cm^{-1} in the irradiated cysteine spectrum is likely due to the S–S stretching mode of the C–SS–C disulfide bridge in cystine (see Fig. 4). Note that the position of the bands due to the S–S stretch are sample dependent, since the ν(S–S) vibrational frequency depends on the variable dihedral angle of the carbon atoms bound to the S atoms in the C–SS–C structure.[35] The peaks at 618 cm^{-1} and 678 cm^{-1} produced by the irradiation are close in wavenumber to the C–C stretch and C–S stretch modes at 616 cm^{-1} and 678 cm^{-1}, respectively, of the cystine reference spectrum shown in Fig. 5 (bottom). As Fig. 6 shows, in the higher Raman shift range from 1080 to

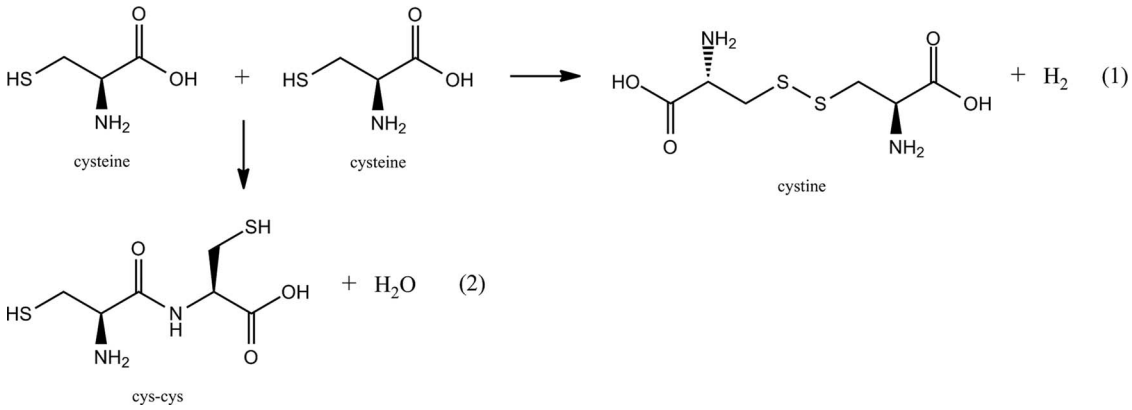

FIG. 4. Possible reaction pathways for linking two L-cysteine molecules when heated.

Downloaded 13 Jun 2013 to 128.171.57.189. This article is copyrighted as indicated in the abstract. Reuse of AIP content is subject to the terms at: http://rsi.aip.org/about/rights_and_permissions

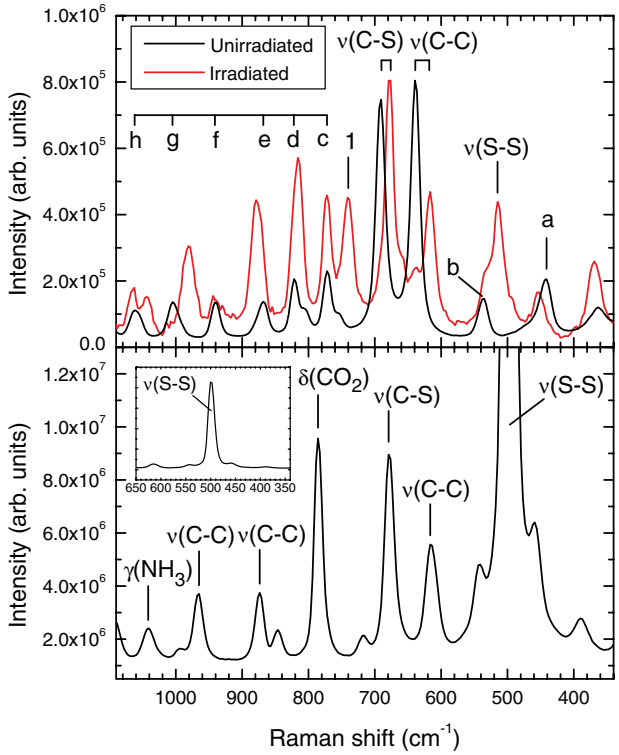

FIG. 5. Raman spectrum of a levitated L-cysteine sample before and after irradiation by the CO_2 laser (top) compared with a reference D-cystine Raman spectrum (bottom). Following irradiation, a new peak appears due to the ν(S–S) stretch mode, and the ν(C–C) and ν(C–S) stretch mode peaks move to higher Raman shifts (see top figure). The unirradiated cysteine peak assignments[33] are a(CCN_{bend}), b($CO_{2\ rock}$), c($CH_{2\ rock}$), d($CO_{2\ wagg}$), e(CC_{str}), f(SH_{bend}), g($NH_{3\ rock}$), and h($NH_{3\ rock}$). The label 1 refers to a peak not clearly present in either the unirradiated L-cysteine or cystine (see text for details). The cystine peak assignments shown are from Ref. 34.

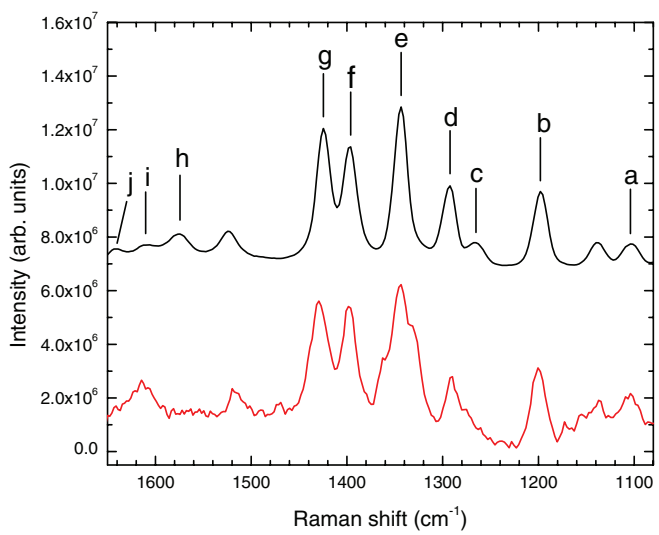

FIG. 6. Raman spectrum of a levitated L-cysteine sample in the 1650–1080 cm^{-1} range before (top spectrum) and after irradiation (bottom spectrum) by the CO_2 laser. The unirradiated cysteine peak assignments,[33] where available, are a(CH_{bend}), b($CH_{2\ twist}$), c(CH_{rock}), d($CH_{2\ wagg}$), e($NH_{3\ sym.\ bend}$), f($CO_{2\ sym.}$), g($CH_{2\ bend}$), h($NH_{3\ asym.\ bend}$), i($NH_{3\ asym.\ bend}$), and j($CO_{2\ asym.\ str.}$). For illustration purposes, the unirradiated spectrum is shown displaced vertically upwards.

1650 cm^{-1} the changes to the cysteine spectrum induced by the laser heating are significantly smaller than displayed in Fig. 5 (top). In particular, there is no clear evidence for the formation of amide I, II, and III bands, which would be expected in the dipeptides at the shifts of approximately 1640, 1530, and 1260 cm^{-1}, respectively.[36] A large background started to appear for longer irradiation times or higher laser powers. Consequently, it was not possible to obtain good quality spectra showing further significant changes than displayed in Fig. 5 (top). In conclusion, the new peaks suggesting the formation of S–S and C–S bonds in the disulfide bridge, and the absence of clear evidence for the production of amide bands, implies that the production of cystine (process 1) rather than the dipeptide bond (process 2) is favoured by the heating process. However, there are new peaks [see, for example, the peak at 740 cm^{-1} labelled 1 in Fig. 5 (top)] that do not appear to correspond to bands in either unirradiated L-cysteine or cystine. Consequently, the irradiated cysteine spectrum is not a simple linear combination of unirradiated L-cysteine and cystine, and therefore the processes induced by the heating are probably more complex than depicted in Fig. 4.

B. Combustion relevant studies: Graphite

As a first step in our goal of studying combustion processes and the growth of organics on carbonaceous particles, we obtained a Raman spectrum from a single grain of graphite levitated in oxygen at atmospheric pressure as shown in Fig. 7. The line at 1577 cm^{-1} is due to the E_{2g} mode, whereas the 1347 cm^{-1} band is attributed to the A_{1g} mode of the lattice produced by the finite crystal size.[37] The two peaks were observed on a fluorescent background, which was reduced significantly by lowering the gate delay from 495 to 470 ns (see Sec. II D). Since the levitator is enclosed within a UHV chamber, the toxic chemicals required for combustion studies can be safely contained. Furthermore, owing to the small heat capacity of the sample and the CO_2 laser power, the levitated

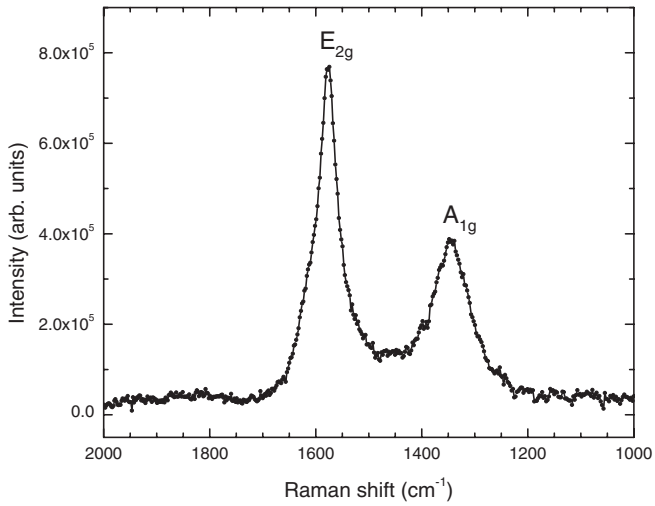

FIG. 7. Raman spectrum showing the E_{2g} and A_{1g} modes[37] of grain of graphite levitated in oxygen.

Downloaded 13 Jun 2013 to 128.171.57.189. This article is copyrighted as indicated in the abstract. Reuse of AIP content is subject to the terms at: http://rsi.aip.org/about/rights_and_permissions

particles can, subject to the stability limitations[28] discussed in Sec. II C, be heated to the high temperatures required for combustion experiments over very short time scales (Subsection 3 of the Appendix).

C. FTIR spectroscopy

Although asymmetric bands superimposed upon a large scattering background are expected for spherical particles with dimensions that can be acoustically levitated (see Sec. II E), there are nevertheless irregularly shaped materials that produce relatively undistorted absorption lines. Three examples of such materials are discussed below, all of which were levitated in anhydrous nitrogen at atmospheric pressure.

1. Polystyrene sheet

The FTIR spectrum of a 38 μm thick, levitated polystyrene $[(C_8H_8)_n]$ sheet with a 2 mm × 2 mm surface area is shown in Fig. 8, where it is compared with a spectrum from the same sample material collected internally within the spectrometer. Although the two spectra in Fig. 8 appear different upon first inspection, we note that the peak positions are the same and mainly the relative peak amplitudes have changed. The differences arise because the polystyrene sheet levitates almost horizontally, so that the IR beam passes through a greater length of material. Therefore, the more intense lines saturate and broaden, such as the region between 2800 cm^{-1} and 3100 cm^{-1}; whereas the relative amplitudes of the smaller features increase, which is especially evident for most of the structure below 2000 cm^{-1}. The enhancement of the relative intensities of the smaller peaks would help to detect small changes in the chemical composition of the levitated sheets. The absorption lines of polystyrene have been assigned in detail in Ref. 38, and hence only selected prominent bands are discussed below. The ring deformation ν(Ph) and bending modes δ(Ph) of the phenyl ring (C_6H_5) produce many, closely spaced bands at wavenumbers below approximately 2000 cm^{-1}. The absorption bands at 2849 cm^{-1} and 2925 cm^{-1} are due to the symmetric $\nu_s(CH_2)$ and asymmetric $\nu_a(CH_2)$ stretching modes of the –CH_2– backbone, respectively. Finally, the three peaks at 3025, 3060, and 3081 cm^{-1} are assigned to the C–H stretching modes ν(Ph) of the phenyl ring. The oscillations in the baseline in Fig. 8 (top), which are clearly visible between 2000 cm^{-1} and 2800 cm^{-1} where there are no prominent absorption lines, are due to the interference between waves internally reflected multiple times within the sheet.

2. Polyethylene sheet

The FTIR spectrum from a levitated sheet of polyethylene $[(C_2H_4)_nH_2]$ is shown in Fig. 9 compared with a standard spectrum from the same sample material collected internally within the spectrometer. For the polyethylene sheet, the more intense peaks are broader and the relative amplitudes of the smaller peaks increase compared to the standard polyethylene sample (cf. Fig. 8). The amplitude of the oscillatory structure is larger in Fig. 9 (top) than for the polystyrene sheet (Fig. 8 (top)) owing to the stronger internal reflections within the polyethylene sheet. The doublet at 720 cm^{-1} and

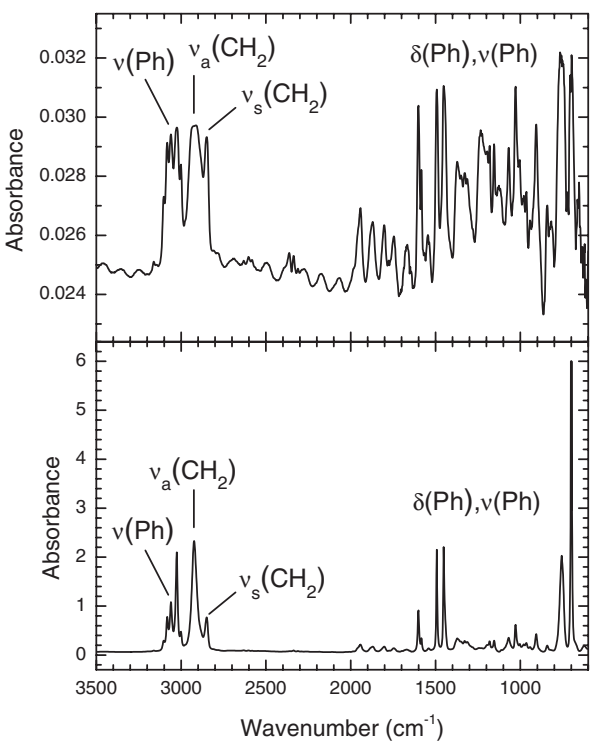

FIG. 8. FTIR spectrum of a 38 μm thick, levitated polystyrene sheet (top) compared to standard spectrum from the same material (bottom). The assignments[38] of selected, prominent vibrational modes are shown (see text for details).

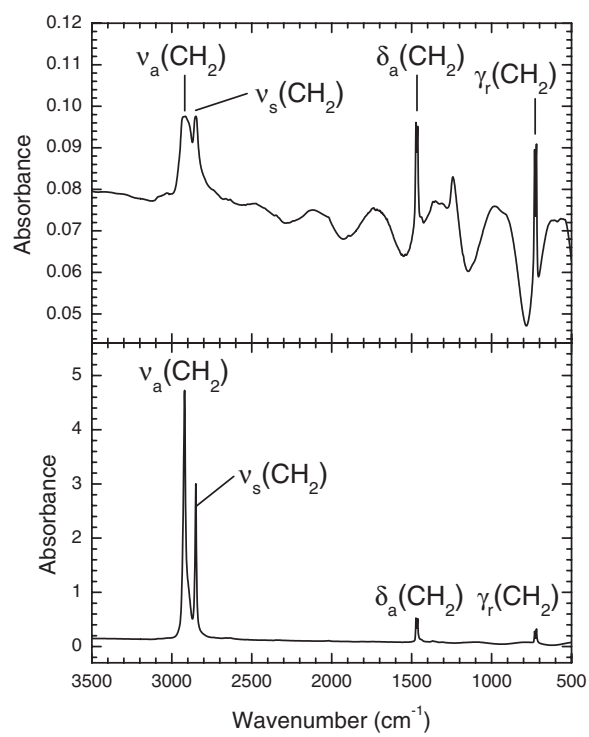

FIG. 9. FTIR spectrum of a levitated polyethylene sheet (top) compared to standard spectrum from the same material (bottom). The assignments[39] of the vibrational modes are shown (see the text for details).

Downloaded 13 Jun 2013 to 128.171.57.189. This article is copyrighted as indicated in the abstract. Reuse of AIP content is subject to the terms at: http://rsi.aip.org/about/rights_and_permissions

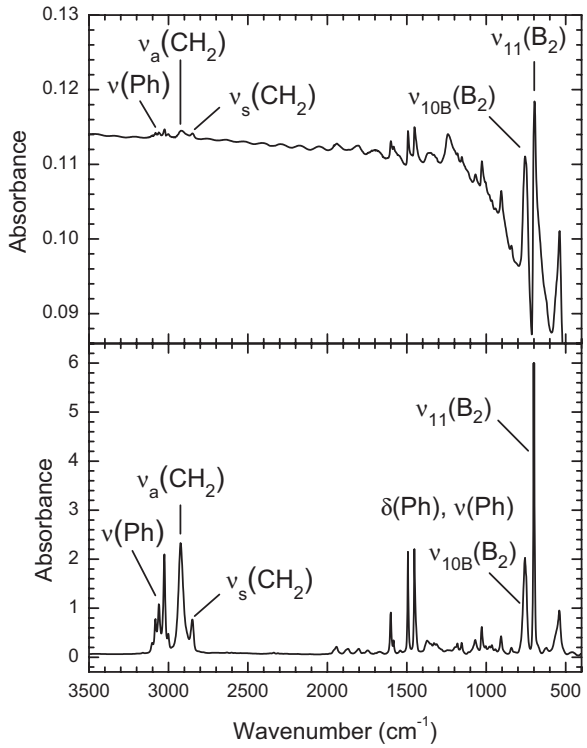

FIG. 10. FTIR spectrum of levitated expanded polystyrene (top) compared to a standard polystyrene spectrum (bottom). The assignments[38] of selected, prominent vibrational modes are shown (see text for details).

735 cm^{-1} is assigned to the $\gamma_r(CH_2)$ rocking mode, and the 1462 cm^{-1} and 1473 cm^{-1} doublet is produced by the $\delta_a(CH_2)$ bending mode.[39] In the higher wavenumber region, the $\nu_s(CH_2)$ symmetric stretch and $\nu_a(CH_2)$ asymmetric stretch modes are observed at 2851 cm^{-1} and 2919 cm^{-1}, respectively.

3. Expanded polystyrene

The spectrum of expanded polystyrene with a diameter of 1 mm is shown in Fig. 10 compared to the same standard spectrum as displayed in Fig. 8 (bottom). At some wavenumbers, there is evidence of asymmetry in the absorption lines such as for the structure at 698 cm^{-1} and 755 cm^{-1} due to the $\nu_{11}(B_2)$ and $\nu_{10B}(B_2)$ out-of-plane deformation modes, respectively.[38] Furthermore, as discussed in Sec. II E, the reduction in the background below approximately 1200 cm^{-1} likely arises from non-resonant scattering.

In summary, the present experimental apparatus is well suited to physically supporting micrometer-thick, flexible sheets. Furthermore, by observing the relatively undistorted absorption lines, the FTIR spectrometer can be used to investigate reactions on the surfaces of these sheets and also porous samples. In addition, we have observed both non-resonant and resonant scattering from an irregular, non-spherical particle.

IV. CONCLUSION

We have described an original apparatus combining an ultrasonic levitator with a pressure-compatible process chamber, carbon dioxide laser heating, and the complementary detection methods of FTIR and Raman spectroscopy. Since the levitator is enclosed within a process chamber, the environmental conditions such as the gas pressure, temperature, and chemical composition can be controlled. To increase the detection efficiency of the FTIR spectrometer, it was necessary to reduce the diameter of the IR beam in the region of the levitated particle. The two standard approaches of beam reduction using a Keplerian or Galilean telescope are unsuccessful for the widely diverging beam from the FTIR spectrometer. We therefore used two optical stages of beam reduction to produce a 4 mm diameter spot in the trap center and thereby increased the detection efficiency by a factor of 130. We described a Raman spectrometer capable of probing the levitated particle from outside of the process chamber with high sensitivity and simultaneously covering the spectral range from 4387 to 168 cm^{-1}. Furthermore, by using a pulsed laser and gated CCD camera, the Raman spectrometer has the advantage of reducing the long-lived fluorescent background and the ambient light component in the spectra. We demonstrated how to levitate a particle using a manipulator operated from outside of the process chamber, and this procedure enables experiments to be performed with the required, possibly toxic, gases.

Ultrasonic levitation has previously been combined separately with a Raman spectrometer, FTIR spectroscopy, and a carbon dioxide laser but, to our knowledge, not all three techniques simultaneously. The combination of the three techniques, the pressure-compatible process chamber, and the advantages of ultrasonically levitating small particles makes novel experiments possible related to, for example, astrobiology, planetary science, and combustion sciences. We showed that the apparatus is well suited to studying the dehydration of a variety of particles including sulfate minerals and biological samples such as the amino acids. For example, we investigated the reaction pathways induced by levitating and heating cysteine, which suggest that oxidation to cystine dominates over dehydration to cysteine dipeptide (cys–cys). At higher temperatures, levitation also offers the possibility of studying combustion processes and, as a first step, we presented the Raman spectrum of a graphite grain.

The FTIR spectrometer was employed to observe non-resonant and resonant light scattering from highly irregular, non-spherical particles, where Mie theory does not accurately represent the scattering functions. Laboratory experiments have been performed previously to obtain the scattering functions of non-spherical particles at a fixed wavelength.[30] In contrast, for our apparatus, we observed the scattering function of irregular particles across the mid-infrared range from 2.5 μm to 25 μm. Although most particles that can be acoustically levitated result in asymmetric absorption bands superimposed upon a large scattering background, we found examples of materials that produce relatively undistorted absorption lines, namely, expanded polystyrene and tens of micrometer thick, microgram sheets of polystyrene and polyethylene. The present experimental apparatus is therefore well suited to physically supporting micrometer thick, flexible sheets and determining the chemical composition of their surfaces by FTIR spectroscopy. The potential applications include studying the surface chemistry of graphene sheets.

Downloaded 13 Jun 2013 to 128.171.57.189. This article is copyrighted as indicated in the abstract. Reuse of AIP content is subject to the terms at: http://rsi.aip.org/about/rights_and_permissions

In the future, the relative humidity of the gas introduced into the process chamber will be varied using a humidity controller or by mixing anhydrous and water-saturated gas in different combinations.[32] It will then be possible to investigate rehydration processes by varying the humidity in the region of the levitated particle. Furthermore, we intend to incorporate a closed-cycle helium refrigerator or liquid nitrogen based cooling system to reduce the temperatures of the buffer gas in the process chamber to those found on the planets and their moons such as Titan. The cooling system will help us explore the condensation of volatile gases of planetary relevance such as water and ammonia onto mineral surfaces.[5,40,41] Thus, the new apparatus will permit future experiments relevant to astrochemistry, planetary chemistry, biochemistry, material science, atmospheric chemistry, and combustion processing.

ACKNOWLEDGMENTS

The material presented in this paper was based upon work supported by the National Aeronautics and Space Administration (NASA Astrobiology Institute under Cooperative Agreement No. NNA09DA77A issued through the Office of Space Science).

APPENDIX: TEMPERATURE OF A LEVITATED PARTICLE

As an example, the temperature of the gypsum crystal discussed in Sec. III A will be determined as a function of the laser power. To make the calculations feasible, we make the approximation that the particle can be represented by a sphere of radius a. We first consider each of the heating and cooling mechanisms for the levitated particle.

1. Heating and cooling processes

a. Power absorbed from the laser

The power absorbed from the CO_2 laser beam by the particle, $P_{abs}(\lambda_l)$, is given by

$$P_{abs}(\lambda_l) = Q_{abs} I_l \pi a^2, \tag{A1}$$

where Q_{abs} is the absorption efficiency of the particle (see Sec. II E for a definition of Q), I_l is the laser intensity or the power per unit area, and λ_l is the wavelength of the IR laser. To calculate I_l, we use 4.9 mm for the radius of the laser beam at the trap center (see Sec. II C). In the limit of geometrical optics ($2\pi a/\lambda \to \infty$), which applies here, the absorption efficiency Q_{abs} is given by[25]

$$Q_{abs} = 1 - Q_{refl}. \tag{A2}$$

The physical interpretation of (A2) is that all of the incident light not reflected enters the particle to be absorbed. The reflection efficiency is given by[25]

$$Q_{refl} = 2\int_0^{\pi/2} R(\theta_i)\cos\theta_i \sin\theta_i d\theta_i, \tag{A3}$$

where $R(\theta_i)$ is the reflectance for the incident light as a function of the angle of incidence, θ_i, and can be calculated using the Fresnel formulae. The value of the refractive index for gypsum to be substituted into the Fresnel formulae can be determined using the Lorentz line parameters from Ref. 42, which at 10.6 μm gives

$$m = n + i\,k = 1.332 + 0.113\,i. \tag{A4}$$

We then obtain

$$Q_{abs}(\lambda_l = 10.6\ \mu\text{m}) = 0.93 \tag{A5}$$

which is substituted into (A1).

b. Power radiated by the particle

The power radiated by a particle of temperature T_p is given by

$$P_{em}(T_p) = 4\pi a^2 \int_0^\infty P(\lambda, T_p)\varepsilon(\lambda) d\lambda, \tag{A6}$$

where the energy flux [J m^{-2} s^{-1}] per unit wavelength of the radiation emitted from the surface is obtained from Planck's law

$$P(\lambda, T_p) = \frac{2\pi hc^2}{\lambda^5\left[\exp\left(\frac{hc}{\lambda k T_p}\right) - 1\right]} \tag{A7}$$

with h denoting Planck's constant, c the speed of light, and k Boltzmann's constant. The emissivity $\varepsilon(\lambda)$ depends on the wavelength and can be calculated using Kirchhoff's law

$$\varepsilon(\lambda) = Q_{abs}(\lambda), \tag{A8}$$

where $Q_{abs}(\lambda)$ is determined as discussed in Subsection 1 a. For simplicity, we use the value for $Q_{abs}(\lambda)$ evaluated at the wavelength λ_m corresponding to the maximum of the Planck distribution (A7). At temperatures relevant to the gypsum experiments, that is, 400 K $< T_p <$ 600 K, $Q_{abs}(\lambda_m) \approx 0.90$. We therefore set ε equal to the fixed value of 0.9. The right-hand side of (A6) then simplifies to the Stefan-Boltzmann form, that is, $4\pi a^2 \varepsilon\sigma\ T_p{}^4$, where σ is the Stefan-Boltzmann constant.

c. Power absorbed from the surroundings

The radiation power absorbed by the particle from the surrounding gas and chamber at the temperature T_g can be calculated using the requirement that, in thermal equilibrium, the absorbed and emitted powers are equal

$$P_{abs}(T_g) = P_{em}(T_g). \tag{A9}$$

The power radiated $P_{em}(T_g)$ can be determined using the procedure discussed in Subsection 1 b of the Appendix. In the calculation, we used the value of $Q_{abs}(\lambda_m = 9.67\ \mu\text{m}) = \varepsilon = 0.94$ corresponding to a gas temperature of 300 K.

d. Cooling by gas collisions

Heat loss by conduction to the surrounding gas is the dominant cooling mechanism of the particle. In the continuum regime applicable here, where the mean free path of the

Downloaded 13 Jun 2013 to 128.171.57.189. This article is copyrighted as indicated in the abstract. Reuse of AIP content is subject to the terms at: http://rsi.aip.org/about/rights_and_permissions

TABLE I. Temperature, T_p, of a 1 mm diameter gypsum particle levitated in nitrogen at atmospheric pressure as a function of the CO_2 laser power.

Laser power (W)	T_p (K)
1.0	353
1.2	363
1.6	383
2.0	402
2.4	421
2.8	439
3.2	456
3.6	474
4.0	491
4.4	507
4.8	522

gas molecules ($\sim 10^{-7}$ m) is much smaller than the particle diameter ($\sim 10^{-3}$ m), the heat loss rate from a spherical particle, $P_{con}(T_g)$, is given by[43]

$$P_{con}(T_g, T_p) = 4\pi a k_g(T_g)(T_p - T_g), \tag{A10}$$

where k_g is the thermal conductivity (or the heat conduction coefficient) of the gas. For N_2 at 300 K,

$$k_g = 0.02583 \text{ W m}^{-1} \text{ K}^{-1}.$$

2. Particle temperature in thermal equilibrium

In thermal equilibrium, the absorbed power and the emitted power are equal, that is,

$$P_{abs}(\lambda_l) + P_{abs}(T_g) = P_{em}(T_p) + P_{con}(T_g, T_p). \tag{A11}$$

The particle temperature can be determined by substituting Eqs. (A1), (A6), (A9), and (A10) into (A11), and then solving (A11) for a given laser power, particle radius, and gas temperature T_g. For example, for the typical values

$$a = 0.5 \times 10^{-3} \text{ m}, \quad T_g = 300 \text{ K},$$

we obtain the particle temperatures shown in Table I.

3. Particle heating and cooling timescales

The temperature of the levitated particle, T_p, as a function of the time, t, is determined by the energy balance equation

$$\frac{4\pi}{3} a^3 \rho_P c_s \frac{dT_p}{dt} = P_{abs}(\lambda_l) + P_{abs}(T_g) - P_{em}(T_p) - P_{con}(T_g, T_p), \tag{A12}$$

where ρ_P and c_s denote the mass density and specific heat capacity of the particle, respectively. The left-hand side of Eq. (A12) represents the rate of change of the internal energy of the particle with respect to time. For a given set of initial conditions, the temperature as a function of time, $T_p(t)$, can be determined by numerically integrating Eq. (A12) with respect to time. The heating and cooling rates of the particle are highly sensitive to the variables involved including the particle radius a and laser intensity I_l. For conditions relevant to soot particles in combustion flames, for example, calculations[43] show that the temperature T_p can rise to a few thousand K in a few tens of ns and cool on timescales $\sim\mu$s. Full details of the calculations and physical processes involved are discussed by Liu *et al.*[43]

[1] T. G. Wang and C. P. Lee, in *Nonlinear Acoustics*, edited by M. F. Hamilton and D. T. Blackstock (Academic Press, San Diego, 1998), Chap. 6.
[2] E. H. Trinh, Rev. Sci. Instrum. **56**, 2059 (1985).
[3] S. Santesson and S. Nilsson, Anal. Bioanal. Chem. **378**, 1704 (2004).
[4] W. J. Xie and B. Wei, Appl. Phys. Lett. **79**, 881 (2001).
[5] N. J. Mason, E. A. Drage, S. M. Webb, A. Dawes, R. McPheat, and G. Hayes, Faraday Discuss. **137**, 367 (2008).
[6] S. J. Brotton and R. I. Kaiser, J. Phys. Chem. Lett. **4**, 669 (2013).
[7] D. Gerlich, Hyperfine Interact. **146/147**, 293 (2003).
[8] K. C. Neuman and S. M. Block, Rev. Sci. Instrum. **75**, 2787 (2004).
[9] E. G. Lierke, Forsch. Ingenieurwes. **61**, 201 (1995).
[10] M. V. Berry and A. K. Geim, Eur. J. Phys. **18**, 307 (1997).
[11] M. D. Barnes, K. C. Ng, W. B. Whitten, and J. M. Ramsey, Anal. Chem. **65**, 2360 (1993).
[12] N. Leopold, M. Haberkorn, T. Laurell, J. Nilsson, J. R. Baena, J. Frank, and B. Lendl, Anal. Chem. **75**, 2166 (2003).
[13] S. Santesson, J. Johansson, L. S. Taylor, I. Levander, S. Fox, M. Sepaniak, and S. Nilsson, Anal. Chem. **75**, 2177 (2003).
[14] J. Schenk, L. Trobs, F. Emmerling, J. Kneipp, U. Panne, and M. Albrecht, Anal. Methods **4**, 1252 (2012).
[15] J. T. Cronin and T. B. Brill, Appl. Spectrosc. **43**, 253 (1989).
[16] A. Ermoline, M. Schoenitz, V. K. Hoffmann, and E. L. Dreizin, Rev. Sci. Instrum. **75**, 5177 (2004).
[17] J. K. R. Weber, D. S. Hampton, D. R. Merkley, C. A. Rey, M. M. Zatarski, and P. C. Nordine, Rev. Sci. Instrum. **65**, 456 (1994).
[18] T. B. McCord, G. B. Hansen, F. P. Fanale, R. W. Carlson, D. L. Matson, T. V. Johnson, W. D. Smythe, J. K. Crowley, P. D. Martin, A. Ocampo, C. A. Hibbitts, and J. C. Granahan, Science **280**, 1242 (1998).
[19] T. B. McCord, G. B. Hansen, and C. A. Hibbitts, Science **292**, 1523 (2001).
[20] A. Gendrin, N. Mangold, J. P. Bibring, Y. Langevin, B. Gondet, F. Poulet, G. Bonello, C. Quantin, J. Mustard, R. Arvidson, and S. LeMouelic, Science **307**, 1587 (2005).
[21] A. Wang, J. J. Freeman, B. L. Jolliff, and I. M. Chou, Geochim. Cosmochim. Acta **70**, 6118 (2006).
[22] H. Richter and J. B. Howard, Phys. Chem. Chem. Phys. **4**, 2038 (2002).
[23] H. Richter, S. Granata, W. H. Green, and J. B. Howard, Proc. Combust. Inst. **30**, 1397 (2005).
[24] R. Whitesides, A. C. Kollias, D. Domin, W. A. Lester, and M. Frenklach, Proc. Combust. Inst. **31**, 539 (2007).
[25] C. F. Bohren and D. R. Huffman, *Absorption and Scattering of Light by Small Particles* (Wiley, New York, 1983).
[26] A. K. Geim, Science **324**, 1530 (2009).
[27] E. H. Brandt, Nature (London) **413**, 474 (2001).
[28] C. P. Lee and T. G. Wang, J. Acoust. Soc. Am. **83**, 1324 (1988).
[29] C. J. Bennett, S. J. Brotton, B. M. Jones, A. K. Misra, S. Sharma, and R. I. Kaiser, "Novel high-sensitivity Raman spectrometer to study pristine and irradiated interstellar ice analogs," Anal. Chem. (to be published).
[30] K. Weiss-Wrana, Astron. Astrophys. **126**, 240 (1983).
[31] P. Bassan, H. J. Byrne, F. Bonnier, J. Lee, P. Dumas, and P. Gardner, Analyst **134**, 1586 (2009).
[32] M. C. Schlegel, K.-J. Wenzel, A. Sarfraz, U. Panne, and F. Emmerling, Rev. Sci. Instrum. **83**, 055101 (2012).
[33] A. Pawlukojc, J. Leciejewicz, A. J. Ramirez-Cuesta, and J. Nowicka-Scheibe, Spectrochim. Acta, Part A **61**, 2474 (2005).
[34] J. K. Lim and S. W. Joo, J. Electroanal. Chem. **605**, 68 (2007).
[35] E. Podstawka, Y. Ozaki, and L. M. Proniewicz, Appl. Spectrosc. **58**, 570 (2004).
[36] E. Podstawka, Y. Ozaki, and L. M. Proniewicz, Appl. Spectrosc. **59**, 1516 (2005).
[37] F. Tuinstra and J. L. Koenig, J. Chem. Phys. **53**, 1126 (1970).
[38] C. Y. Liang and S. Krimm, J. Polym. Sci. **27**, 241 (1958).
[39] D. I. Bower and W. F. Maddams, *The Vibrational Spectroscopy of Polymers* (Cambridge University Press, Cambridge, 1989).
[40] S. Bauerecker and B. Neidhart, J. Chem. Phys. **109**, 3709 (1998).
[41] D. A. Williams and E. Herbst, Surf. Sci. **500**, 823 (2002).
[42] L. L. Long, M. R. Querry, R. J. Bell, and R. W. Alexander, Infrared Phys. **34**, 191 (1993).
[43] F. Liu, K. J. Daun, D. R. Snelling, and G. J. Smallwood, Appl. Phys. B **83**, 355 (2006).

Downloaded 13 Jun 2013 to 128.171.57.189. This article is copyrighted as indicated in the abstract. Reuse of AIP content is subject to the terms at: http://rsi.aip.org/about/rights_and_permissions